Fuel 361 (2024) 130735

Contents lists available at ScienceDirect

Fuel

journal homepage: www.elsevier.com/locate/fuel

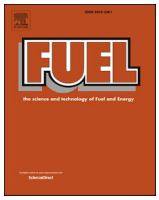

Full Length Article

Soot and PAH formation in laminar diffusion flames of RP-3 jet kerosene and its surrogates at preheat temperature

Shirong Xin, Wenyu Wang, Fan Yang, Yong He, Yanqun Zhu, Zhihua Wang *

State Key Laboratory of Clean Energy Utilization, Zhejiang University, Hangzhou 310027, PR China

ARTICLE INFO

Keywords:
PLII/PILF
soot/PAH formation
Temperature dependence
Aviation kerosene
Surrogate fuels

ABSTRACT

For investigating the effects of preheat temperature on the soot/PAH formation of RP-3 kerosene surrogates, planar laser-induced incandescence (PLII), planar laser-induced fluorescence of PAH (PAH-PLIF) and chemical kinetic simulation are conducted in several laminar diffusion flames. The goal is to provide a surrogate that matches well with the soot formation characteristics of RP-3 kerosene and to investigate the mechanism behind the temperature sensitivity of different surrogates. Firstly, surrogate S1 (30.3% n-hexadecane, 39.8% *iso*-cetane, 29.8% o-xylene, in mole fraction) is formulated to obtain a surrogate with good reproducibility of soot formation characteristics corresponding to the RP-3 jet kerosene. Compared with another reported surrogate S2, S1 presents a higher soot yield due to its higher PAH formation and a stronger soot formation propensity. With elevated preheat temperature, soot yield of all the studied flames gets higher, and the temperature sensitivities for soot formation of S1 and S2 are shown with little difference. By further analyzing the PAH results experimentally and numerically, the temperature sensitivity for soot yield of S2 is more closely related to the temperature sensitivity of PAH precursors, while the subsequent processes after soot inception may be more important to the temperature dependence of S1.

1. Introduction

Soot and PAHs (polycyclic aromatic hydrocarbons) have multiple and proven harmful effects on the earth environment, human health, and operation efficiency of the combustion equipment [1–4]. Soot and PAHs can be produced in virtually any combustion equipment burning with hydrocarbon fuels, such as boilers, vehicle engines, as well as aero-engine combustors. As emission regulations become increasingly strict, emissions of the soot and PAH are also under close scrutiny, including in the aviation industry [5,6]. Understanding and predicting the formation of soot and PAH from aviation fuels is a prerequisite for reducing soot and PAH emissions in the aero-engine combustors. But as the most widely used aviation fuel, aviation kerosene contains hundreds of complex components and the physicochemical properties also show differences because of the different origins and production processes. So it is unrealistic to directly simulate and predict the soot/PAH emission characteristics of real aviation kerosene.

Formulation of surrogate fuel is a solution to achieve high similarity for some combustion characteristics of the aviation kerosene by preparing a mixture of several simple hydrocarbons in a specific ratio. The surrogate formulation method has been widely used for the verification of some combustion characteristics of jet kerosene such as laminar combustion velocity, fuel viscosity, ignition delay time, the sooting tendency, etc. [7–11]. However, as for RP-3 jet kerosene, a jet fuel widely used in aero-engines in China, with higher aromatic content (usually ~ 30 %) than Jet-A or JP-8, the effectiveness of its surrogates is fully verified for several fuel characteristics like laminar combustion velocity [12–14], but the evaluation for the soot/PAH formation characteristics is rarely reported. Gao, Z et al. [15] and Pelucchi et al. [16] has confirmed that the aromatics dominated the sooting tendencies of surrogates due to the domination of PAHs yield, but the further discussions like sensitivity at preheat temperature, are deficient.

Importantly, in order to evaluate the temperature dependence of soot formation, the gas preheat temperature is often set as an important research condition [17–22]. In the actual aero-engine combustor, the air is always preheated to a higher temperature by the multi-stage compressor before it is injected into the burner and mixed with the fuel for combustion. Thus, given its significance in actual combustion conditions, the effects of preheat temperature on the soot/PAH formation of the kerosene surrogate fuels need to be further evaluated, and

* Corresponding author.
E-mail address: wangzh@zju.edu.cn (Z. Wang).

https://doi.org/10.1016/j.fuel.2023.130735
Received 24 May 2023; Received in revised form 20 November 2023; Accepted 22 December 2023
Available online 25 December 2023

temperature sensitivity can be derived experimentally and numerically to investigate the further influence of compositional effects on the sensitivity of soot yield, as an in-depth evaluation for the surrogates.

The temperature sensitivity of soot formation represents the rate of change in the soot growth rate with higher preheat temperature. It is an assessment for the temperature dependence of soot growth of a certain fuel, which is closely related to the soot formation propensity of the fuel itself. The temperature sensitivities of simple alkanes, olefins and aromatic hydrocarbons has been well investigated in the co-flow diffusion flames of the previous studies [17–19]. The enhancement of soot loading at elevated temperature is well verified, but for this enhancement, different fuels exhibit very different mechanisms. For simple alkanes and olefins, the fuel unsaturation determines the temperature sensitivity of soot formation due to the difference of PAH growth rate by early pyrolysis [18], while for aromatics, the PAH yield no longer affects the temperature sensitivity [19]. However, the temperature sensitivity of soot yield of complex mixtures has not been studied. Whether the temperature sensitivity of a mixture is affected by its compositions is still a speculation. Thus, temperature sensitivities of the kerosene surrogate fuels with different matching strategies need further discussion. Besides, as the most important soot precursors, the analysis of temperature sensitivity based on the PAH formation mechanism will help to understand the soot generation sensitivity of kerosene surrogates.

Based on the above research requirements, PLII, PAH-PLIF and chemical kinetic simulation were conducted in this study at different preheat temperatures for the co-flow diffusion flames of RP-3 surrogates. The three main objectives of this work are: (1) to formulate a kerosene surrogate with good reproducibility of soot formation characteristics corresponding to the actual RP-3 jet kerosene; (2) to study the effects of preheat temperature on the soot/PAHs formation of the surrogates by using this surrogate and another reported surrogate as the study objects; (3) to identify the governing factors of temperature sensitivity for the soot/PAH formation of kerosene surrogates.

2. Methodology

2.1. Burner and flames

The method of surrogate formulation for RP-3 kerosene will be described in the Section 3 and the subject of experimental interest in this work is two surrogate fuels (S1, S2) with different strategies of fuel formulation.

The self-designed gas preheat burner is shown in Fig. 1 and the device components are illustrated in detail in our previous paper [17,18]. The burner can provide co-flow of hot air at different temperatures throughout the sooting flame. The high temperature can be maintained with little change within 5 cm above burner outlet and shows uniformity within 2 cm radius of the burner centerline, which guarantees the credible variable of the gas preheat temperature. The outlet fuel temperature is essentially the same as the co-flow temperature due to sufficient heat exchange between the jet tube and the co-flow hot gas. The co-flow temperature is controlled by two electrical heaters and measured by a S-type thermocouple above the burner. The co-flow air flowrate is kept at 50 L/min. As for the fuel supply, an injection pump is used for controlling the liquid fuel flowrate with accuracy of 0.157 g/h. In order to compare the soot generation characteristics of different surrogate fuels, the liquid fuel flowrate is kept at 4.56 g/h and the carbon atom input flow (m_c) of all diffusion flames is kept consistent at 1.084 mg/s. A heater is set at 300 ℃ to evaporate the liquid fuel and N_2 is used as carrier gas, kept at 200 mL/min. The experiment conditions are shown in Table 1. Two gas preheat temperatures (575 K and 675 K) are set for the RP-3, S1, and S2. According to the calculation results provided in the Supplemental Information, early thermal decomposition of S1 and S2 can be observed over 750 K. Below 675 K, the fuel vapor inside the burner jet tube is less prone to thermal decomposition. Additionally, the volume fraction of the diluted N_2 is much larger than that of the fuel vapor in order to keep the studied flames from smoking. This is beneficial for experimental observations and analyses.

2.2. Optical diagnostics

2.2.1. Planar laser-induced incandescence (PLII)

Fig. 1 shows the arrangement of the soot-PLII measurement system described in our previous paper [18]. A slight difference is that, a 532 nm laser from a 10 Hz Nd:YAG laser (Powerlite DLS 8010, Continuum) is used as the excitation laser for LII. The laser energy density was kept at 0.14 J/cm^2 to guarantee that LII signal was in the saturation region, and to avoid high-temperature soot sublimation resulting in incandescent intensity decay. Then a concave lens ($f = -30$ mm) and a convex lens ($f = +500$ mm) were applied to form a laser sheet with a height of 5 cm and a waist thickness of 200 μm. The soot LII signal was captured by the ICCD camera (PI-max4 emICCD, Princeton Instrument) equipped with a Nikon ultraviolet lens (PF10545MF-UV) and a narrow-band filter (Edmund, central wavelength = 400 nm, FWHM = 25 nm). The ICCD gate width was kept at 100 ns. The time interval between the laser beam and the ICCD camera gate was maintained at 100 ns, for preventing soot

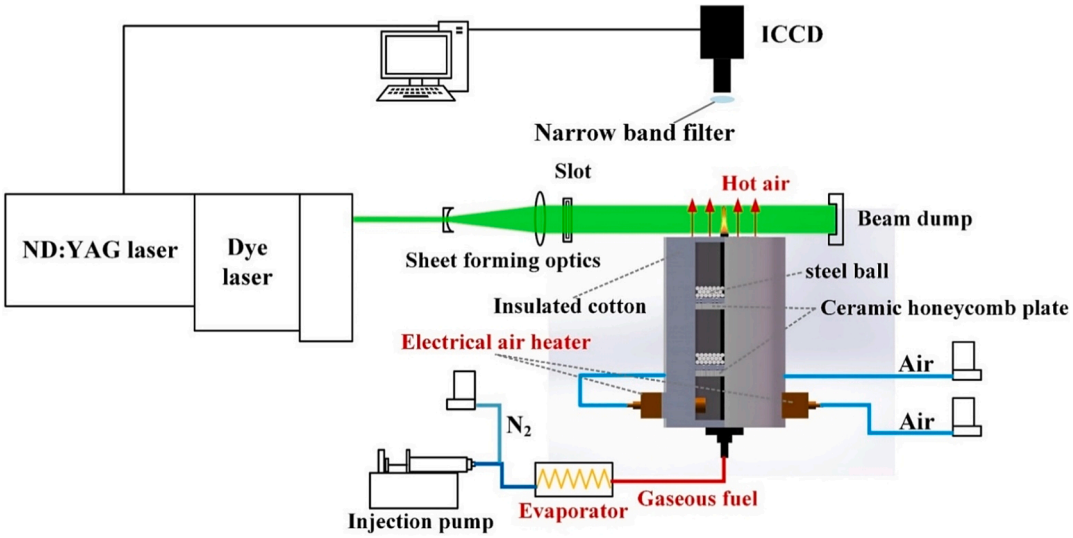

Fig. 1. PLII/PLIF measurement system and gas preheat burner setup.

Table 1
All recorded experiment conditions.

Fuel			Carrier gas	Co-flow	T_{air} (K)	575	675
	Flowrate (g/h)	Vapor flowrate (mL/min)	N_2 (mL/min)	Flowrate (SLM)	v_{air} (m/s)	0.200	0.235
RP-3	4.56	18.4	200	50	T_{fuel} - T_{air} (K)	3	5
					T_{ad} (K)	–	–
S1	4.56	18.8	200	50	T_{fuel} - T_{air} (K)	2	3
					T_{ad} (K)	2223 (2412)	2279 (2456)
S2	4.54	23.9	197	50	T_{fuel} - T_{air} (K)	4	5
					T_{ad} (K)	2227 (2409)	2284 (2452)

T_{ad}: the resultant adiabatic temperatures of stoichiometric flames calculated in the CHEMKIN's Equilibrium model. Values in parentheses are T_{ad} for jet-fuels without nitrogen diluent.

LII signal from interference of PAH laser-induced fluorescence due to the excitation laser at visible wavelength [23]. The 400 nm band filter also helped to reduce the fluorescence interference from other flame species when performing PLII measurement [24]. A beam extinction measurement was performed to acquire a calibration coefficient for converting LII intensity to f_v, and the setup details are the same as our previous work [17].

2.2.2. Planar laser-induced fluorescence of PAHs (PAHs-PLIF)

PAHs-PLIF was conducted for qualitative measurement of PAHs fluorescence. The setup of PAHs-PLIF was similar to the PLII system. A 10 Hz Nd:YAG laser (Powerlite DLS 8010, Continuum) was used to excite Rhodamine 590 dye to produce 283 nm laser after second harmonic. The 283 nm laser was tuned to avoid excitation of hydroxyl radicals. And the laser pulse energy for PLIF was kept at 2.5 mJ to prevent obvious LII excitation. PAHs fluorescence signals were collected by ICCD camera with a gate width of 50 ns. Although the 283 nm laser failed to excite fluorescence of the one-ring aromatic hydrocarbons, other kinds of PAHs were unaffected [25]. According to previous research [26–30], a 327–353 nm bandpass filter (Edmund, central wavelength = 340 nm, FWHM = 26 nm) was used before the ICCD camera to collect the fluorescence of A2 (two-ring aromatics), and a 373–400 nm bandpass filter (Edmund, central wavelength = 386 nm, FWHM = 27 nm) was used for A3 (three-ring aromatics) measurement. 200 collected images were required for each working condition and raw PLIF images were corrected according to background noise and the spatial energy distribution of the laser sheet. Additionally, a 513–538 nm bandpass filter (Edmund, central wavelength = 525 nm, FWHM = 25 nm) was used for Visible-LIF measurement. It should note that the LIF in visible wavelength band may encompass emissions from many complex soot precursors, such as five-membered ring PAHs [31], bridged-PAHs [32], dimeric PAHs [27], or nano-particles [33,34], which are intermediate products in the transition from simple gaseous PAHs to solid soot in the soot nucleation process, representing precursor species intimately associated with soot nucleation reactions. Since there is still no consensus on the mechanism of soot nucleation, "Visible-LIF" is used in this paper to reflect the fluorescence of soot nucleation precursors to illustrate the effects of preheat temperature on the soot nucleation process.

2.2.3. Two-color thermometry measurement

Two-color thermometry measurement is applied for soot temperature imaging and the detail is described in our previous paper [17,18]. Two ultra-narrow band filters (Andover, central wavelength = 532 nm & 647 nm, FWHM = 1 nm) were used for the ICCD camera to collect the soot luminosity with a gate width of 5 ms. The planar distribution reconstruction of the soot luminosity image relied on the Abel transform [35]. Then the reconstructed luminosity signals were applied to calculate the soot temperatures. When calibrating, a B-type thermocouple (Pt/30 % Rh-Pt/10 % Rh) was placed above a Bunsen flame of methane at the burner center. The temperature of the 100 μm thermocouple junction was recorded and at the same time, luminosity signals of the junction recorded by the ICCD camera were used to calculate the calibration coefficient.

2.3. Chemical kinetic modeling

Chemical kinetic simulations were performed based on the Diffusion Opposed-flow Flame Model in CHEMKIN-PRO software [36]. This 1-D model has been commonly used in several publications for simulating the detailed chemical kinetic reactions of diffusion flame [15,37]. For the above reason, Diffusion Opposed-flow Flame Model was adopted in this work to analyze the PAHs formation characteristics of kerosene surrogate fuels. The CRECK mechanism developed by Ranzi et al. [38] was applied for gas phase reaction simulation. This mechanism contains 249 species and 8153 reactions, which are up to C20 species. In the CHEMKIN-PRO simulation setup, the fuel mass flowrate, temperature, and fuel compositions were consistent with the experiment setup, but the air mass flowrate was kept at one third of the actual co-flow flowrate to ensure the combustion process at a low strain rate. The distance between the outlets of fuel and oxidizer is set to 3.6 cm. The simulation conditions included practical experiment conditions of S1 and S2 at different gas preheat temperatures. The counter-flow flame model can be used to analyze the general trends of sooting tendency but it should be noted that the composition-time trajectories vary with the location in jet diffusion flames and this complexity can't be captured via counter-flow flame simulations.

3. Surrogate formulation and evaluation

3.1. Surrogate fuel formulation

The first step for surrogate fuel formulation is the components analysis. Fig. 2 shows the gas chromatography - mass spectrometry (GC–MS, Thermo Fisher Scientific) results of the RP-3 jet kerosene used

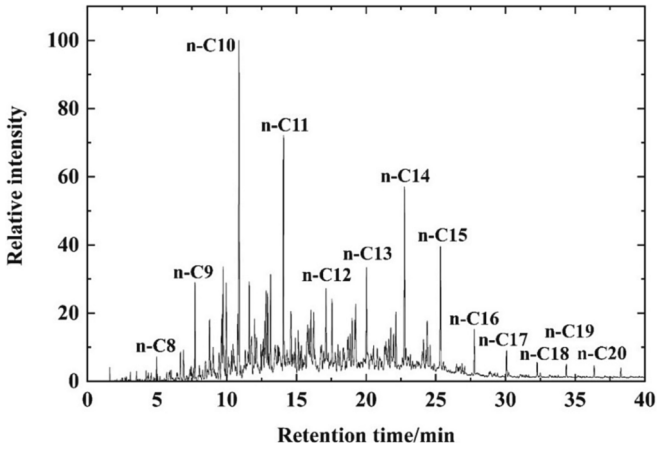

Fig. 2. GC–MS result of the RP3 jet kerosene used in this work.

in this paper. The RP-3 jet kerosene mainly consists of alkanes and aromatics. The carbon number distribution ranges from C7 to C27, with the distribution of alkanes ranging from C8 to C20, which indicates the RP-3 kerosene in this work includes some heavy components probably due to its origin and production process. Although the molecular weight is up to 194.85, other physical properties like lower heat value or cetane number meet the national standards of RP-3 aviation kerosene [39]. The formula of the RP-3 kerosene is calculated to be $C_{13.9}H_{28.08}$.

In this paper, given the physicochemical properties and hydrocarbon groups composition of several single fuels, n-hexadecane, *iso*-cetane, and o-xylene are chosen as the surrogate components. In order to match the properties of surrogate fuel and jet kerosene such as the gas-phase diffusion characteristics, heat release property, fuel reaction enthalpy and soot formation property, the molecular weight (MW), lower heat value (LHV), H/C ratio, threshold sooting index (TSI), cetane number (CN), and density are applied as the selection index of the surrogate fuel formulation. The calculation equations [8] of these six selection indexes and the objective function of the optimization problem are as follows. These selection indexes have the linear combinations of pure components, which are used in many studies [7–9,12,13] on liquid-fuel surrogate formulation methods.

Calculation equations of different selection indexes:

$$MW_{mix} = \sum_i x_i MW_i \tag{1}$$

$$LHV_{mix} = \sum_i w_i LHV_i \tag{2}$$

$$H/C_{mix} = \frac{\sum_i x_i N_{H_i}}{\sum_i x_i N_{C_i}} \tag{3}$$

$$TSI_{mix} = \sum_i x_i TSI_i \tag{4}$$

$$CN_{mix} = \sum_i v_i CN_i \tag{5}$$

$$\rho(T)_{mix} = \sum_i v_i \rho(T)_i \tag{6}$$

Objective function:

$$F = \sum_{j=1}^{6} \left[C_j \left(\frac{P_{RP-3} - P_{mix}}{P_{RP-3}} \right) \right]^2 \tag{7}$$

In equations (1)–(7), x_i is the molar fraction of component i, w_i is the mass fraction of component i, v_i is the volume fraction of component i, N_{H_i} is the number of hydrogen atoms of component i, N_{C_i} is the number of carbon atoms of component i, P_{RP-3} is the selection index of RP-3, P_{mix} is the corresponding selection index of components, C_j is the weight of each selection indexes which is set as 1/6. When F is at a minimum value during the iteration, the concentration of each components is output. Finally, the calculated surrogate fuel S1 composes of 30.3 % n-hexadecane, 39.8 % *iso*-cetane, 29.8 % o-xylene (in mole fraction). The physical properties of the RP-3, surrogate components, and surrogate fuels are shown in Table 2. In addition, the surrogate fuel S2 (14 % n-decane, 10 % n-dodecane, 30 % *iso*-cetane, 36 % methylcyclohexane, 10 % toluene) is according to the RP-3 kerosene formulation in ref [12].

3.2. Experimental measurement results

Fig. 3 shows the 647 nm soot luminosity images of the laminar co-flow diffusion flames of RP-3, S1 and S2. The luminosity images reflect the area of soot distribution and the diffusion flame length. It can be found that the distribution area, flame length and flame brightness of S1 present a high similarity compared to RP-3 at any preheat temperature, which preliminarily suggests the effectiveness of surrogate fuel formulation in soot formation and the similarity of the soot radiant heat release between RP-3 and S1.

Table 2
Selection indexes value of the RP-3, surrogate components, and surrogate fuels.

Selection indexes value	RP-3	n-hexadecane	*iso*-cetane	o-xylene	S1	S2 [12]
MW (g/mol)	194.85	226.44	226.44	106.17	190.55	149.4
LHV	42.34	43.95	43.85	40.8	43.38	44.06
H/C	2.02	2.13	2.13	1.25	1.97	2.045
TSI	25.87	8.58	22	47	25.38	–
CN	45	100	15	8.3	44.81	41.52
viscosity (mm^2/s, 20 °C)	2.38	4.27	4.69	0.92	2.8	–
density (g/cm^3, 20 °C)	0.79	0.79	0.78	0.86	0.8	–

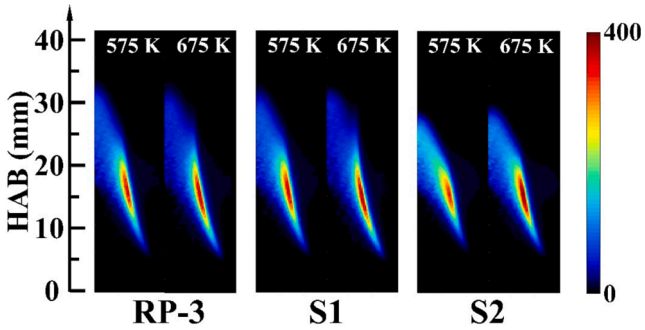

Fig. 3. Soot luminosity images recorded at the wavelength of 647 nm for the laminar co-flow diffusion flames of RP-3, S1 and S2. The images are deconvolved by Abel transform.

Fig. 4 presents the LII results of soot volume fraction (f_v) along the centerline and pathline (axial line at r = 2.5 mm). The data are derived from the 2D images which can be found in Supplemental Materials. As shown in the figure, the axial soot volume fraction shows a high similarity between the RP-3 and S1 at two preheat temperatures, including the start height of soot formation, the maximum f_v, the end height, which reveals the good reproducibility of the surrogate S1 in terms of the axial f_v distribution characteristics of the RP-3 kerosene. The pathline f_v profiles are axial cuts at a radius that includes the position of wing region of the flames, appropriately explaining the soot tendency at the flame wing sides.

LII results of radial f_v along different heights above burner (HAB) are shown in Fig. 5. Within a certain flame, the figures show that the peak soot concentration is much higher upstream (at or below HAB of 16 mm) of the flame than downstream, and the maximum f_v throughout the flame occurs on the wing side below approximately HAB of 20 mm. As HAB increases, the peak gradually moves closer to the burner centerline (r = 0 mm). In general, there is still a good correspondence between S1 and RP-3 in terms of soot formation characteristics of the radial f_v distribution. Overall, S1 can simulate the f_v distribution characteristic of RP-3 kerosene very well.

Fig. 6 presents the fluorescence intensity distributions of A2, A3 and Visible-LIF at different positions in the flames. For the RP-3 flames, due to the PAHs (like naphthalene, 1,3-dimethylnaphthalene, phenanthren [25]) contained in the jet kerosene itself, strong signals of the kerosene LIF are already observed at the outlet of the jet tube, and the intensities of these signals drown out other signals from combustion. It is indistinguishable between the A2 and A3 signals generated during the combustion of jet kerosene and those originating from the inherent kerosene constituents, and the production of PAHs can't be quantified specifically within the kerosene flames. So the shorter-wavelength

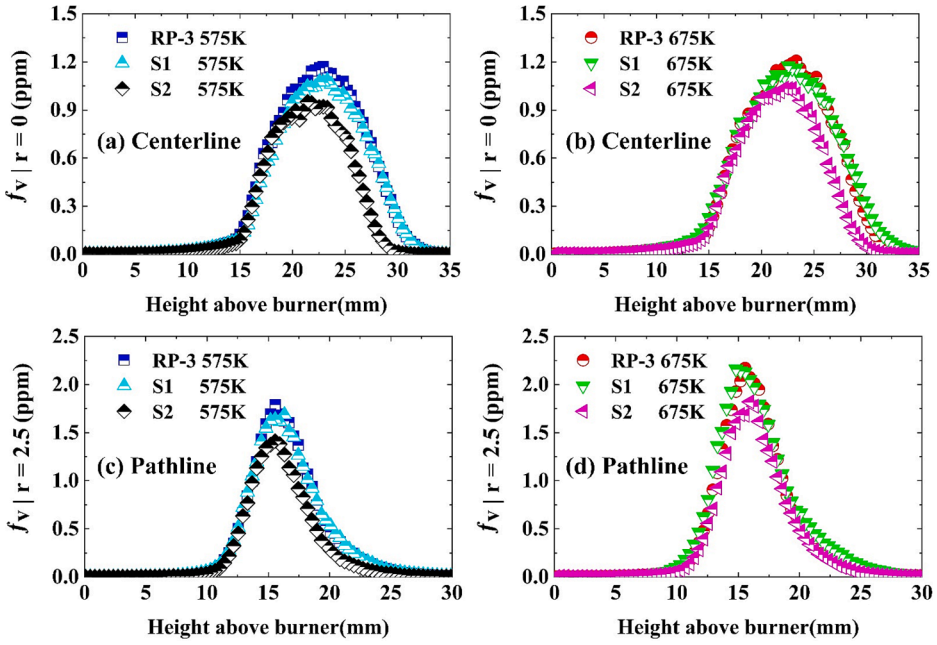

Fig. 4. The measurements of axial soot volume fraction (f_v) along the (a) (b) centerline r = 0 mm and (c) (d) pathline at r = 2.5 mm for the diffusion flames of RP-3, S1 and S2 at different preheat temperatures.

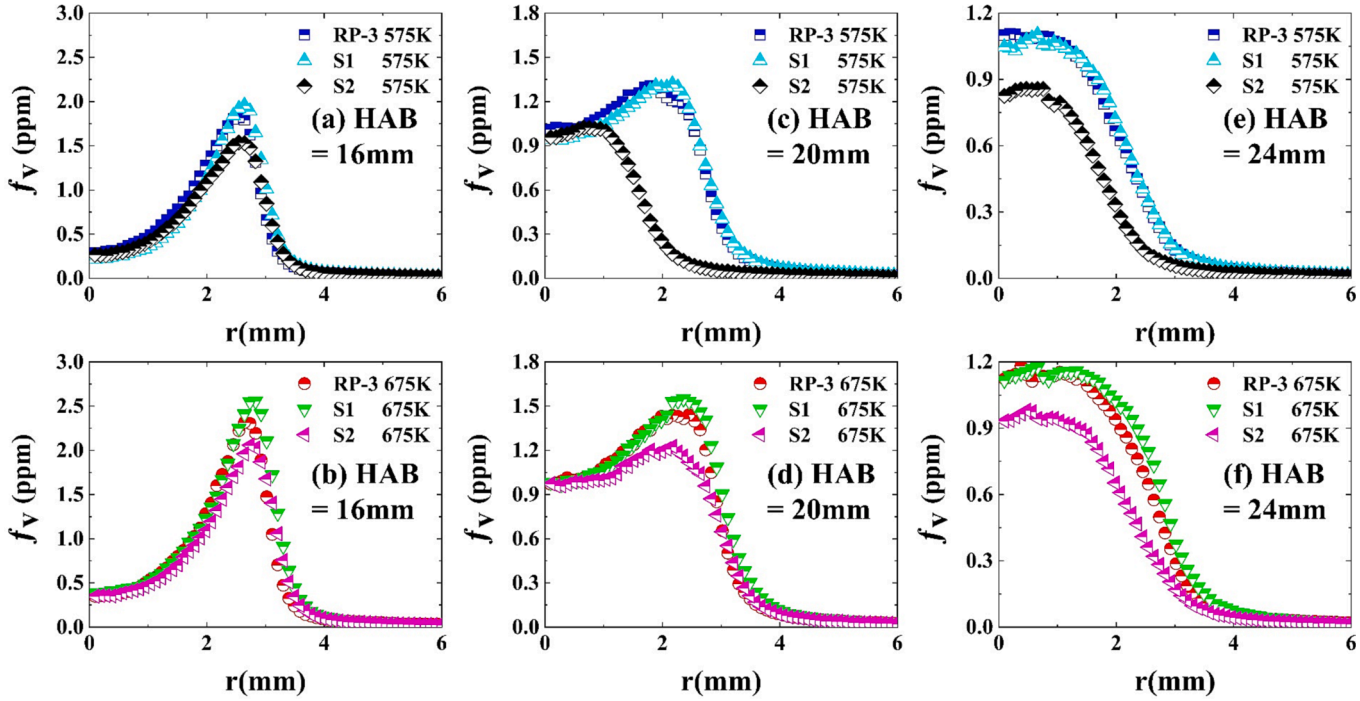

Fig. 5. The measurements of radial soot volume fraction (f_v) alone different heights above burner (HAB) of (a) (b) 16 mm, (c) (d) 20 mm and (e) (f) 24 mm for the diffusion flames of RP-3, S1 and S2 at different preheat temperatures.

fluorescence signals of kerosene won't be analyzed here. However, the intensity of its Visible-LIF away from the UV fluorescence region is essentially similar to that of S1. Given the fact that the detection fluorescence wavelength is sensitive to the PAH size and structure, it is worth noting that the fluorescence in visible range is closely linked to many complex soot nucleation precursors. Some large precursors are generated through E-bridged reactions [32] stimulated by five-membered ring PAHs, and some are nano-particles probably the polymers of PAHs. The mechanism of soot nucleation appears to be currently inconclusive, but anyway, to some extent, the Visible-LIF can be treated as the tracers for soot nucleation processes. Interestingly, no advance generation of Visible-LIF is observed at the exit of the jet tube. So most of the Visible-LIF is generated during combustion. This indicates that the formation of light PAHs doesn't severely affect the formation of larger PAHs, and for the surrogate S1, it can be speculated that the simulation effectiveness of the f_V distribution characteristics may not be related to the initial light PAH, but probably to the process of the soot nucleation or the soot surface growth after the formation of light PAHs. As for this

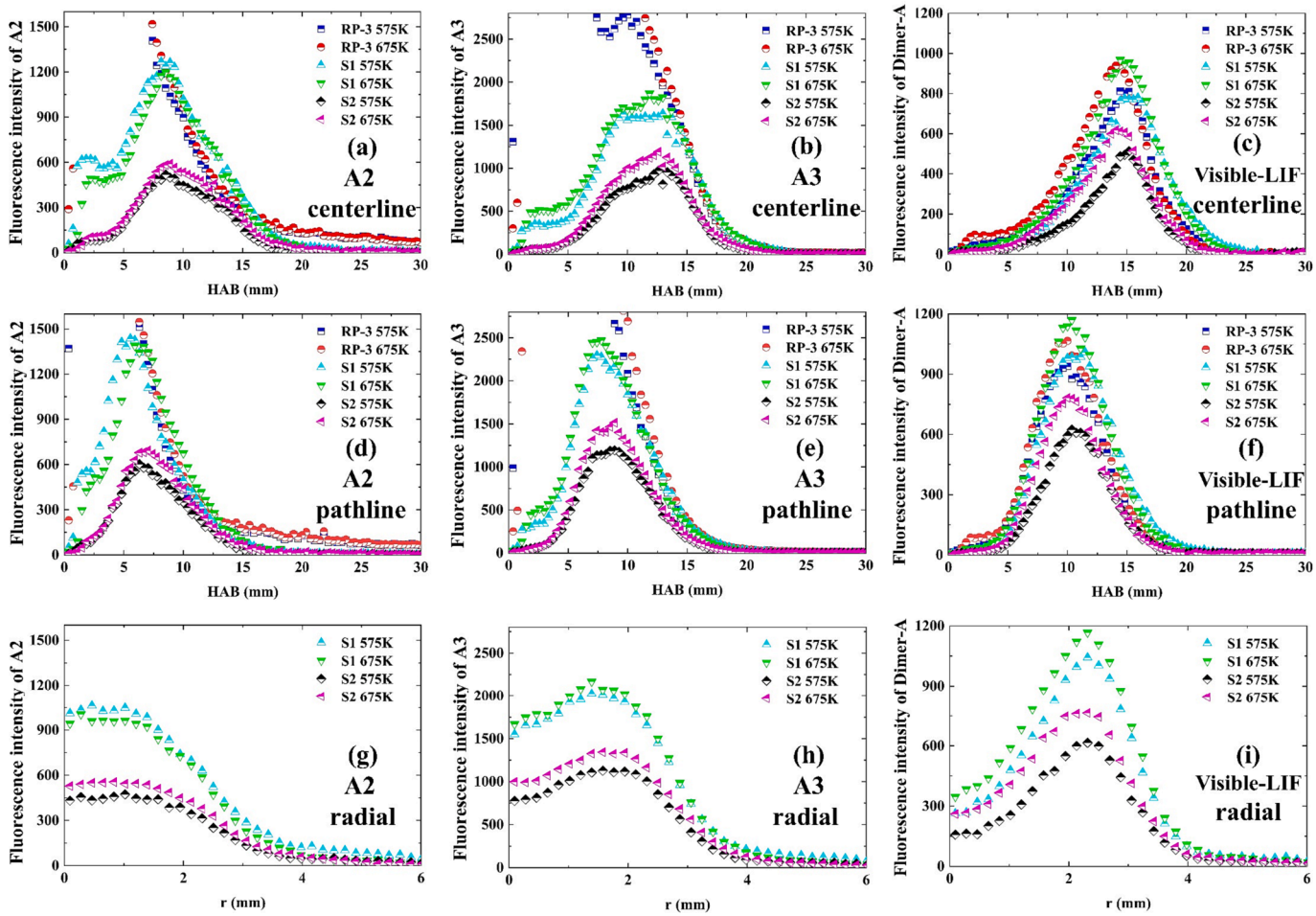

Fig. 6. Fluorescence intensity distributions of A2, A3 and Visible-LIF at (a), (b), (c) centerline, (d), (e), (f) pathline, and (g), (h), (i) radial line (HAB = 10 mm).

type of jet fuel with strong sooting tendency, the soot formation seems to be probably not sensitive to formation processes of the initial PAH like A2 or A3.

4. Surrogates and preheat temperature

After formulating a surrogate matching well with the soot distribution characteristics, the discussion for effects of preheat temperature can be proceeded.

4.1. Effects on soot temperature

As seen in Fig. 3, the soot distribution zone is clearly divided into a thin, narrow wing zone and an inner smooth zone. The flame length and brightness of S1 don't change obviously with the increased preheat temperature, while the brightness of S2 shows a relatively increase only at the wing side. This means an obvious change in soot radiant heat release at the wing side of S2 flames.

The flame temperature in Fig. 7 is corrected according to the position

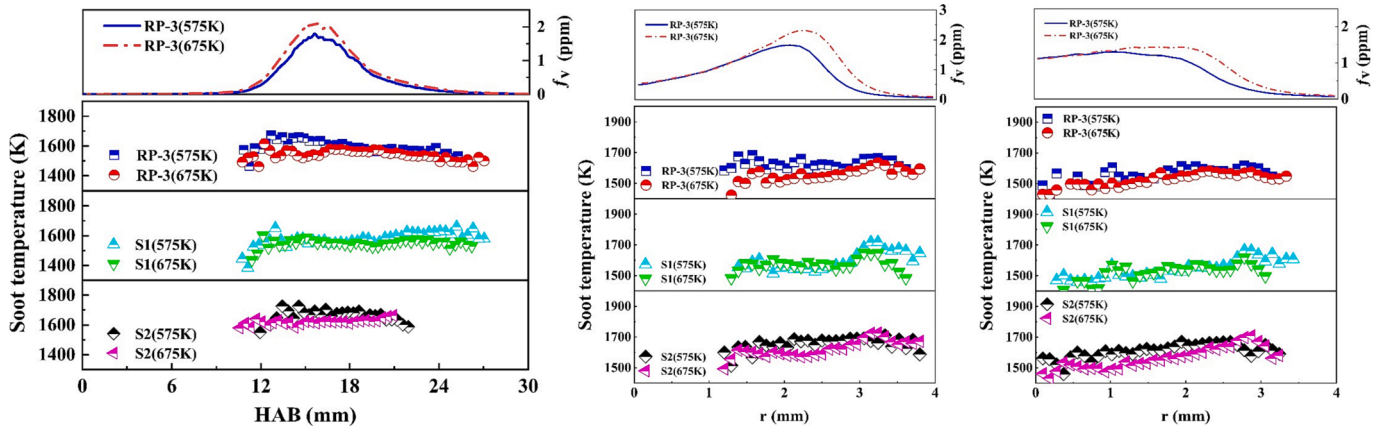

Fig. 7. The results of two-color thermometry contain (a) axial soot temperature at r = 2.5 mm (b) radial soot temperature at HAB = 16 mm and (c) radial soot temperature at HAB = 20 mm. The top figures are the corresponding profiles of f_v distribution.

variation of camera system, the emissivity variation for the thermocouple materials, and the variation in soot emissivity [40]. As shown in Fig. 7 (a), with more preheat energy introduced into the flames, the axial soot temperature doesn't show an increase as expected for all flames, but some slightly decrease presents in the soot temperature at mid-profile instead. According to the analysis in previous studies [18], although the preheat temperature adds extra heat to diffusion co-flow flames, but the soot loading will increase at the same time, and the radiant heat loss of flame will also increase. Jet fuels are fuels with strong sooting tendency and the overall flame temperature of the studied flames already reaches the temperature window (~1400 K) [17,18] at the initial height of soot inception. When the preheat temperature raises, due to radiant energy losses in the parts of the flames with the strongest soot volume fractions (seen in the top of Fig. 7), the axial soot temperature at mid-profile slightly reduces in all studied flames despite the added heat from higher preheat temperature. Correspondingly, no obvious change is found in the brightness of the inner region in these flames. A difference is the wing region of the S2 flames. Results of radial temperature profiles (Fig. 7 (b) and (c)) show that the temperature of S2 at the thin wing side ($2.8 < r < 3.2$ mm) doesn't drop as much as RP-3 and S1 with the increased preheat temperature. This is consistent with the LII results that the S2 flames have lower soot concentrations in wing region than S1. Because lower sooting fuel like S2, forms soot at higher temperatures than S1 or RP-3 and has lower soot radiant losses, which corresponds to the increase in the brightness of S2 wing region with higher preheat temperature.

4.2. Effects on soot volume fraction (f_v)

With higher preheat temperature, the S1 f_v in the Fig. 4 shows no significant change along the centerline but shows a relatively rapid increase along the pathline. The enhancing effect of gas preheat temperature on f_v is relatively remarkable in pathline zone. Due to the proximity of the pathline region to the flame front, more energy is provided for soot formation at the wing side, as analyzed by Chu et al. [20] and Smooke et al. [41]. Compared with S2, the S1 f_v at any flame positions is always higher at the same preheat temperature, which means the higher soot loading in the overall S1 flames. The higher radial f_v peak of S1 in Fig. 5 also suggests the stronger soot growth at the wing side in S1 flames than S2, which corroborates the previous analysis in the soot temperature.

The carbon conversion factor η was used to evaluate the propensity of fuel to soot, which represents the percentage of carbon converted to soot [42]. The calculation equations of η are as follows:

$$\eta = \frac{m_s}{m_c} \tag{8}$$

$$m_s = v_h \rho_s \int 2\pi f_v(r,h) r dr \tag{9}$$

$$v_h = (v_{fuel}{}^2 + 2ah)^{\frac{1}{2}} \tag{10}$$

$$t = \frac{v_h - v_{fuel}}{a} \tag{11}$$

where m_c is the total mass flow rate of carbon, kept at 1.084 mg/s for all flames mentioned in Section 2.2. m_s is the mass flow rate of carbon converted to soot, calculated by the axial velocity v_h (derived by Roper et al. [43,44]), the soot particle density ρ_s (set as 1900 kg/m^3 [45]), and the row integral of soot volume fraction at a certain height. Soot residence time t is determined by the axial velocity, the initial fuel velocity v_{fuel}, and the buoyancy acceleration a (constant at ~ 25 m/s^2 [46]).

Fig. 8 presents the results of carbon conversion factor η versus soot residence time t. Although the total mass flow rate of carbon is kept the same for S1 and S2, the carbon conversion factor of S1 is always higher than that of S2 at any preheat temperatures. It has been confirmed that the aromatics provide a tremendous promoting effect on sooting tendencies of surrogates due to the promotion of the soot inception step [15]. Thus, the carbon conversion capacity is probably determined by the percentage of aromatic hydrocarbons in the surrogates (29.8 % in S1, 10 % in S2). Importantly, for all the studied flames, the soot yield increases with more preheat energy introduced into the flames, indicating the more carbon converted to soot. It can be found that the influence of preheat temperature is similar in these three fuels, since the higher temperature speeds up the decomposition and reorganization of the jet fuel in the flame, which promotes the soot inception and growth, ultimately contributing to the enhanced soot loading. When the preheat temperature increases by 100 K, the maximum η increases by a factor of 1.25 for RP-3, 1.37 for S1, and 1.35 for S2. The total soot loading $f_{v|vol\text{-}int}$ increases by a factor of 1.36 for RP-3, 1.62 for S1, and 1.56 for S2. The maximum soot volume fraction $f_{v,max}$ increases by a factor of 1.33 for RP-3, 1.44 for S1, and 1.27 for S2. The specific values of these indexes

Table 3
Key indexes of soot formation characteristics of the RP-3 and surrogate fuels.

Type of jet fuel	RP-3		S1		S2	
Preheat temperature (K)	575	675	575	675	575	675
Maximum η	0.0664	0.0832	0.0668	0.0917	0.0567	0.0767
Total soot loading $f_{v\|vol\text{-}int}$ (ppm × mm^3)	5773	7830	5609	9088	4122	6449
$f_{v,max}$ (ppm)	2.01	2.68	2.02	2.9	1.63	2.07

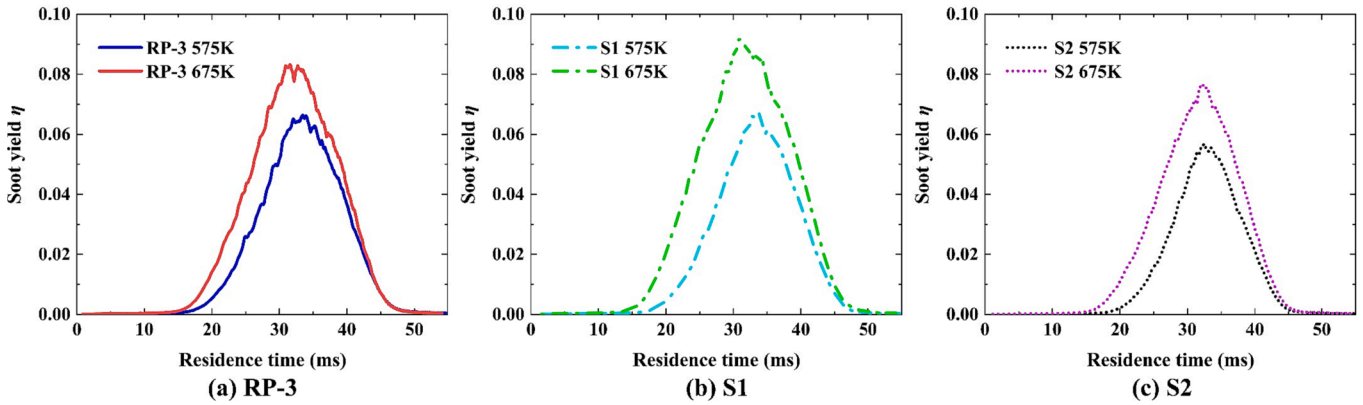

Fig. 8. Percentage of carbon converted to soot, i.e., carbon conversion factor η versus soot residence time for RP-3, S1 and S2 at different preheat temperatures.

are listed in Table 3. But on the other hand, these change of soot growth rate is different for the two surrogates, which implies a difference in their temperature sensitivity. This difference will be explained in the final section.

4.3. Effects on PAH formation

Fig. 9 and Fig. 10 present the simulation results of some key chemicals in the 1-D diffusion opposed-flow flames of S1 and S2. Compared with S2, the higher soot loading of S1 is probably due to its higher A2-A4 concentration, which means the stronger soot nucleation for S1. As shown in the figures, the A2-A4 mole fraction are all higher in S1 flames at any temperatures. This is consistent with the difference in experimental LIF intensity of A2/A3 in S1 and S2 flames (Fig. 6). Besides, due to the higher Visible-LIF intensity in S1 flames, the soot nucleation reactions in S1 flames are also probably stronger than S2.

Importantly, the effect of preheat temperature is similar both the numerically and experimentally. In Fig. 9 and Fig. 10, the concentrations of all the key components related to the soot formation increase at the elevated preheat temperature. The PLIF results of A3 and Visible-LIF in S1 and S2 flames (Fig. 6) also support this point, although there is a slight decrease for A2 fluorescence upstream of the S1 flame at 675 K due to the interference from o-xylene fluorescence with faster decomposition at higher temperature. But obviously, all the reaction rates enhance at the higher temperature and this enhancement of PAH formation is probably related to the alkanes with higher content in the surrogates, because there is essentially no change of the PAH concentration in the aromatic flames with elevated preheat temperature, as reported in previous literature [19]. However, according to the PLIF results (Fig. 6), compared with S2, the enhancement of PAH-LIF in S1 flame is very limited, indicating the temperature sensitivity of A3 or Visible-LIF is also different and the temperature dependence of PAH formation needs to be discussed.

5. Temperature dependence

The sensitivity of soot growth of different fuels to the change in heat of the preheated gas depends on the soot formation propensity of the fuel itself. This propensity depends on the formulation of the fuel compositions which have different soot formation mechanisms.

Temperature sensitivity based on maximum carbon conversion factor η was used to evaluate the temperature dependence of soot yield of a certain fuel in several studies [17,19]. The temperature sensitivity is derived from the slope of the curve of the maximum η versus preheat temperature, which represents the rate of change in the soot growth per unit preheat-temperature. Fig. 11 (a) presents the temperature sensitivity k for the soot yield of two surrogates. For alkanes, the H/C ratio and unsaturation together affect the temperature sensitivity. For aromatics, due to the presence of their own benzene rings, the reaction about forming the first aromatic one-ring is no longer the rate-determining step of PAH formation and thus not sensitive to the elevated temperature, and thus the formation reactions of larger PAHs like pyrene are also not temperature-sensitive [19]. Generally, the temperature sensitivities of different large-molecular alkanes don't differ much but are all higher than that of aromatic hydrocarbons. Interestingly, S1 has much higher aromatic content than S2, but in Fig. 11 (a), its temperature sensitivity of soot yield is slightly higher than S2 instead. Fig. 11 (b) and (c) presents the experimental temperature sensitivity of PAH formation based on the fluorescence intensity of Visible-LIF and A3. The results contain two kinds of temperature sensitivity of PAH formation based on the $S_{PAH,int}$, the total integrated PLIF intensity and the $S_{PAH,max}$, the maximum row-integral PLIF intensity, respectively. As seen in the results, the temperature sensitivity for PAH formation of S2 is greater than that of S1 for both $k(S_{PAH,int})$ and $k(S_{PAH,max})$, indicating that the PAH formation rate increases more easily for S2 than S1 if the same heat is introduced into the flame. Compared with S2, S1 exhibits inertia in the PAH generation reactions at elevated temperature.

Simulation results for the temperature sensitivity of PAH formation also validate the experimental PLIF results. Fig. 12 presents simulation results of the normalized peak mole fraction of some precursors versus preheat temperatures. The normalization is based on the simulated mole fraction at 475 K, and the slope represents the temperature sensitivity. As shown in the figure, the temperature sensitivities of A2, A3 and A4 of S2 are greater than those of S1, and the more the number of benzene rings on the PAH molecule, the larger the difference. This suggests that the process of soot inception in S2 flame is more susceptible to the change in gas preheat temperature. Compared with S1, the temperature sensitivity of soot yield of S2 is more closely related to the temperature sensitivity of the PAH precursors growth, while the temperature

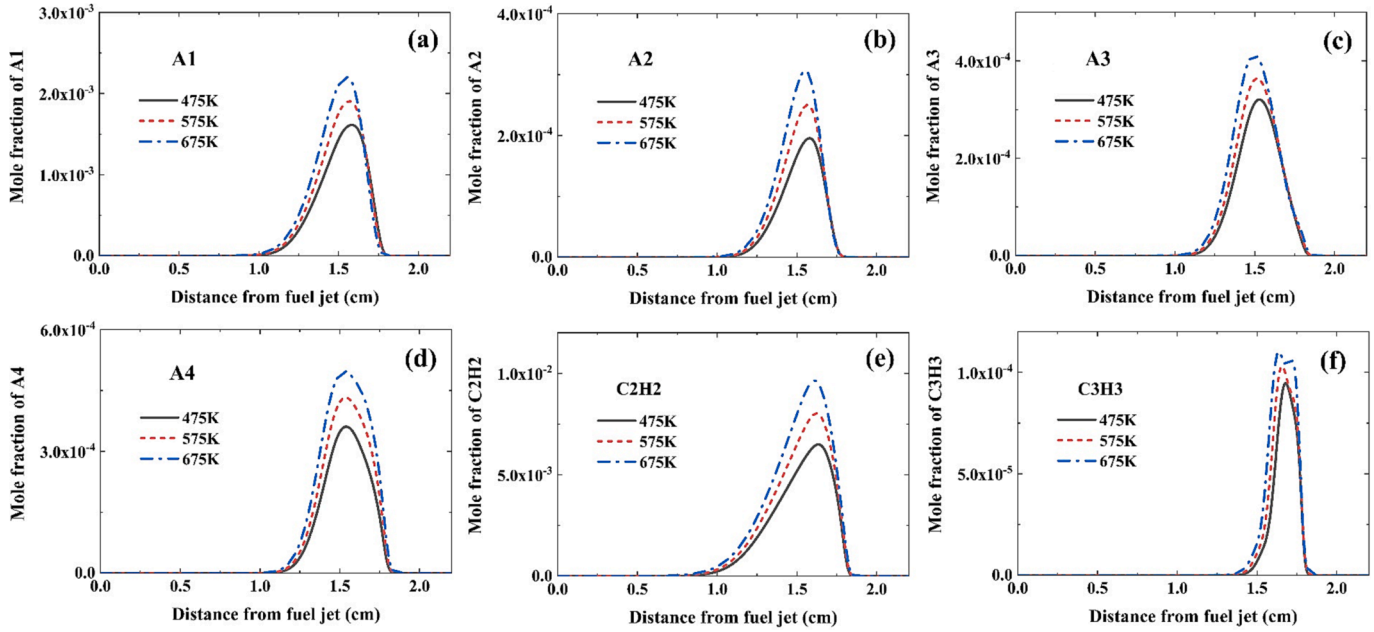

Fig. 9. Simulation results of (a) A1, (b) A2, (c) A3, (d) A4, (e) C2H2, (f) C3H3 in the S1 flames.

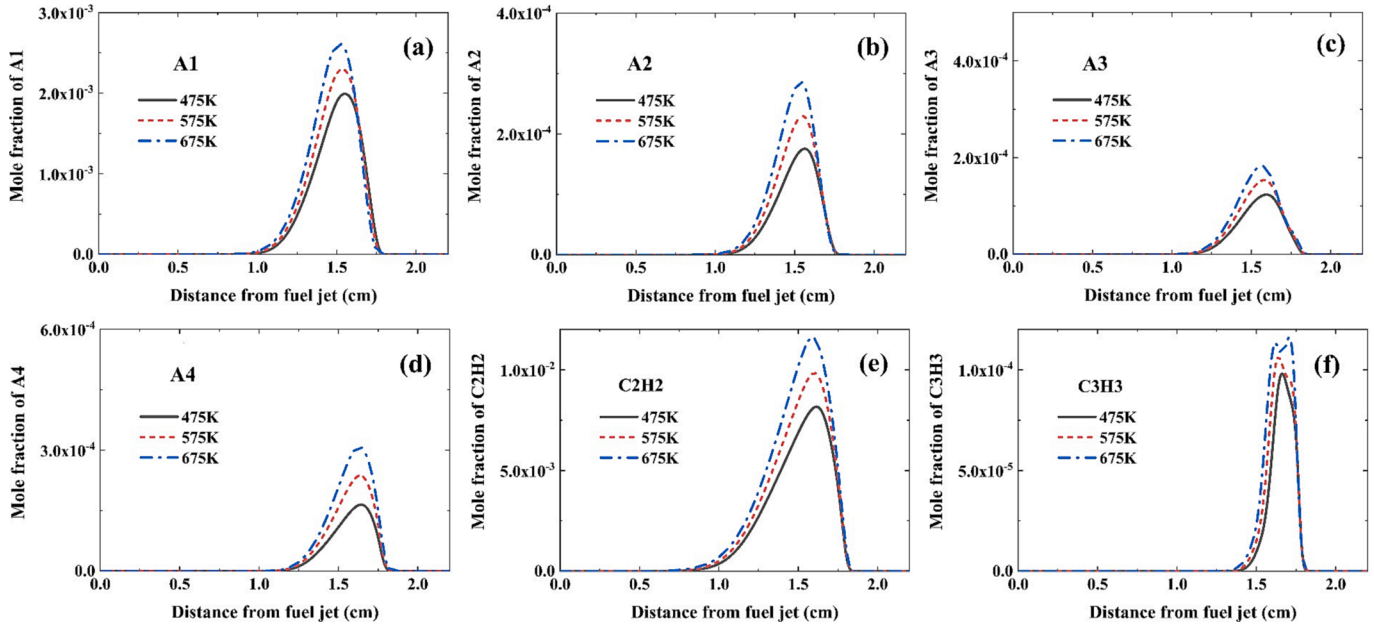

Fig. 10. Simulation results of (a) A1, (b) A2, (c) A3, (d) A4, (e) C2H2, (f) C3H3 in the S2 flames.

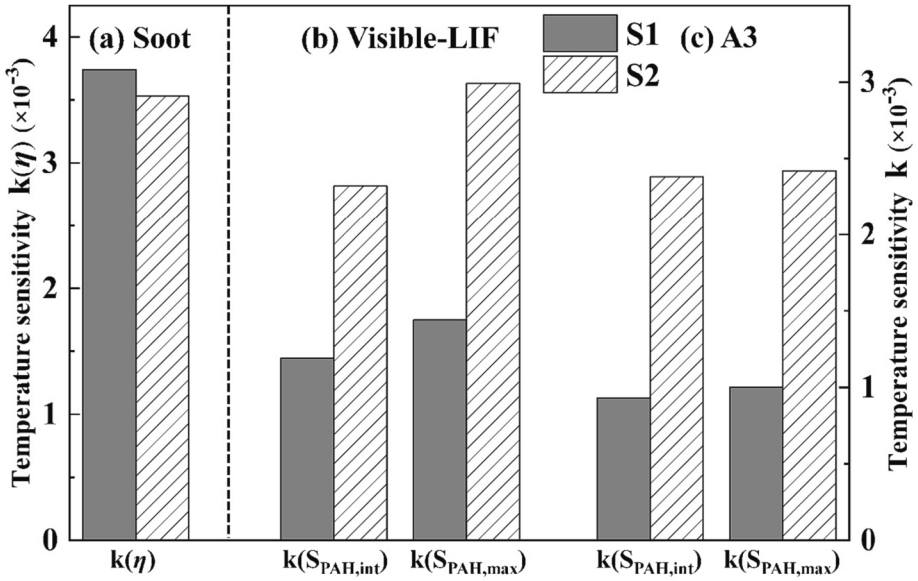

Fig. 11. (a) Temperature sensitivity k of different fuels based on maximum carbon conversion factor η. (b) & (c) are temperature sensitivity k of PAH formation based on the fluorescence intensity of Visible-LIF and A3, respectively. $S_{PAH,int}$ means the total integrated intensity of a certain PAH. $S_{PAH,max}$ means the maximum row-integral intensity of a certain PAH.

sensitivity of soot yield of S1 is probably more dependent on the sensitivity of subsequent processes, such as soot surface growth, PAH absorption, and soot oxidation. For example, according to the Fig. 12 (e) and (f), the temperature sensitivities of C2H2 and OH of S1 is slightly greater than those of S2. C2H2 is an important participant in the soot surface growth mainly by HACA (Hydrogen-abstraction-C2H2-addition) mechanism [47], while OH is related to the oxidation of the soot particles [48]. In general, the rate of HACA surface growth depends on the C2H2 concentration and temperature [49], while the rate of PAH absorption depends on the PAH concentration. For the S1 sooting flames, the faster increase in C2H2 and the higher formation of PAHs may lead to a high temperature sensitivity in the subsequent processes of soot formation in S1 flame, in spite of the relatively low temperature sensitivity in PAH yield. Thus, the subsequent processes after soot inception may appear to be more important in terms of the soot temperature dependence of S1.

To further explain the difference in temperature sensitivity of PAH formation mechanism between S1 and S2, Fig. 13 presents the simulated peak rates of production (ROP) for control reactions of A2, A3, A4 formation with different preheat temperatures. The peak rates of production are normalized according to their own values at 475 K. The control reaction is defined as the reaction whose ROP contribution ranks the first in a certain PAH. For S1, the primary control reaction of A2 is R936, and A3 and A4 are controlled mainly by R1031.

$$C3H3 + RXYLENE => A2 + CH3 + H \quad \text{(R936)}$$

$$2RXYLENE => 0.5A4 + 0.5A3 + 2H2 + CH3 + H \quad \text{(R1031)}$$

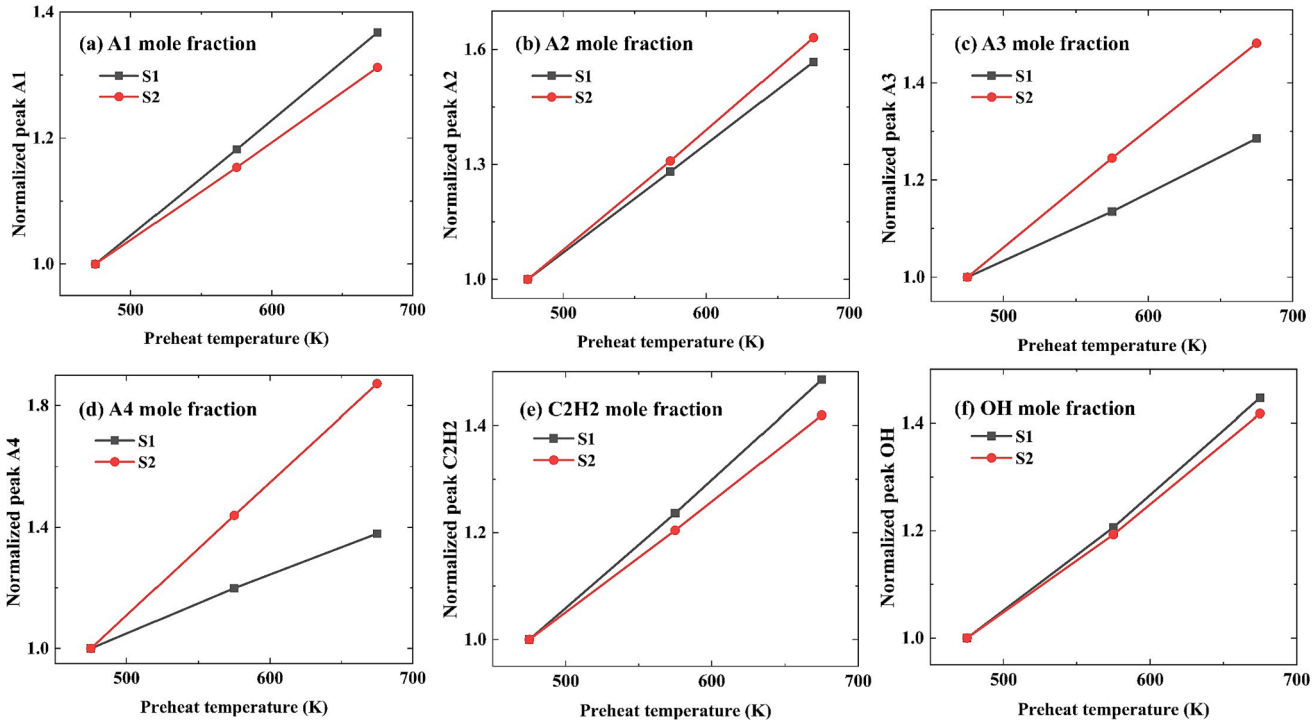

Fig. 12. Simulation results of the normalized peak mole fraction of some key precursors during soot formation versus preheat temperatures. The slope of the curve represents the temperature sensitivity of precursors growth of the surrogates.

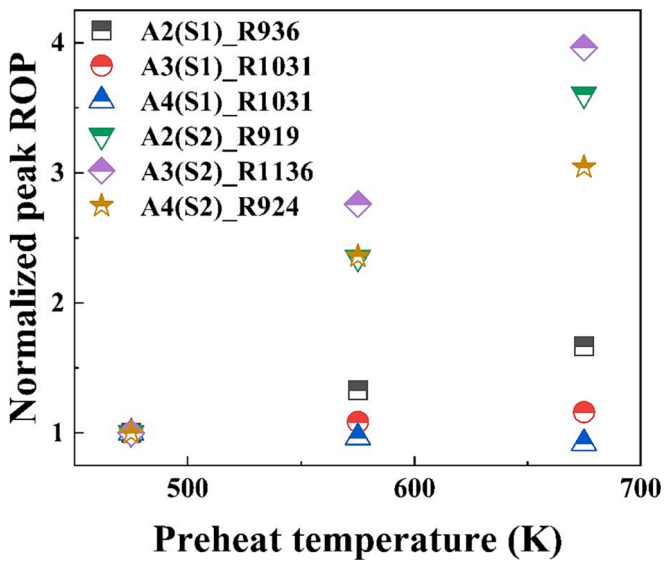

Fig. 13. Normalized peak rates of production (ROP) for control reactions of A2, A3, A4 formation, with different preheat temperatures.

For S2, R919 is the main control reaction for A2, R1136 for A3 and R924 for A4.

$$HC2A1- + C2H2 => A2 \quad (R919)$$

$$HC2A1- + A1 => A3 + H \quad (R1136)$$

$$A3- + C2H2 <=> A4 + H \quad (R924)$$

From the above reactions, it is clear that the o-xylene (29.8 % in S1, in mole fraction) dominates the PAH formation of S1 flames, proceeding to the next formation step of PAH precursors. Although the global reaction R1031 needs to be treated carefully, the reaction $H + XYLENE = > H2 + RXYLENE$ is found very sensitive to the production of A3 and A4, indicating a significance effect of xylene radicals on the A3/A4 formation. However, the PAH formation in S2 flames depends mainly on the gradual addition of benzene ring dominated by the alkanes (90 %) in S2. In particular, all the S2 control reactions have little correlation with toluene (10 %) in S2. Like $HC2A1-$ in R919 and R1136, mostly are generated from small radicals in radical pool produced by alkane decomposition without passing through toluene. Its control reaction is R884 ($C2H2 + A1- <= > H + A1C2H$) where all the A1 are directly generated in radical pool (mainly the combination of C3H3). For alkanes, the formation of the first benzene ring must be preceded by decomposition, and these decomposition reactions are more sensitive to the reaction temperature. Therefore, as shown in the Fig. 13, with elevated preheat temperature, all the peak ROP of S2 control reactions increases but the increase for peak ROP of S1 control reactions almost all stagnates. For the surrogate S2 with lower aromatic content, the PAH temperature sensitivity behaves more like an alkane, while the S1 behaves more like an aromatic hydrocarbon. Thus, for the formulation of kerosene surrogate, the aromatic content not only determines the soot yield, but also the temperature sensitivity of soot precursor formation.

6. Conclusions

In order to investigate the effects of preheat temperature on the soot/PAHs formation of RP-3 kerosene surrogates, PLII, PAH-PLIF and chemical kinetic simulation are conducted for several co-flow diffusion flames. The contribution of this article is providing a surrogate that can match the soot formation characteristics of RP-3 kerosene and investigate the mechanism for temperature sensitivity of different surrogates. The conclusions are drawn as follows:

(1) Compared with RP-3 jet kerosene, the formulated surrogate S1 (30.3 % n-hexadecane, 39.8 % *iso*-cetane, 29.8 % o-xylene, in mole fraction) presents a good similarity in formation characteristics of soot volume fraction and Visible-LIF, which can be

served as a surrogate with good reproducibility of soot formation characteristics.

(2) The soot temperature of S2 at the wing side doesn't drop as much as S1 at higher preheat temperature, and higher soot yield is found in S1due to its higher PAHs formation, which means S1 presents a stronger soot formation propensity than S2.

(3) Soot yield of all the studied flames gets higher with the elevated preheat temperature, but the temperature sensitivities for soot formation of S1 and S2 are shown with little difference, while the temperature sensitivities for PAH formation of S2 are higher than that of S1.

(4) The temperature sensitivity for the soot yield of S2 is more closely related to the temperature sensitivity of the PAH precursors, while the processes after soot inception like soot surface growth appear to be more important in terms of temperature dependence of S1.

(5) Control reactions related to aromatic hydrocarbon dominate the PAH formation of surrogate with higher aromatic content. For the S2 with low aromatic content, the PAH temperature sensitivity behaves more like that of an alkane, while the S1 behaves more like an aromatic hydrocarbon. This work can give guidance for kerosene surrogate formulation if the soot/PAH emission at practical industrial condition of preheat temperature is concerned.

CRediT authorship contribution statement

Shirong Xin: Writing – original draft, Formal analysis, Data curation. **Wenyu Wang:** Writing – review & editing. **Fan Yang:** Writing – review & editing. **Yong He:** Writing – review & editing, Investigation. **Yanqun Zhu:** Validation, Software. **Zhihua Wang:** Writing – review & editing, Validation, Methodology, Investigation, Conceptualization.

Declaration of competing interest

The authors declare that they have no known competing financial interests or personal relationships that could have appeared to influence the work reported in this paper.

Data availability

Data will be made available on request.

Acknowledgments

This work was supported by National Natural Science Foundation of China (52125605) and the Zhejiang Provincial Natural Science Foundation of China (LR23E060001). Authors also thank the support from the Fundamental Research Funds for the Central Universities (2022ZFJH04).

Appendix A. Supplementary material

Supplementary data to this article can be found online at https://doi.org/10.1016/j.fuel.2023.130735.

References

[1] Shiraiwa M, Selzle K, Poeschl U. Hazardous components and health effects of atmospheric aerosol particles: reactive oxygen species, soot, polycyclic aromatic compounds and allergenic proteins. Free Radic Res 2012;46(8):927–39.
[2] Bond TC, Doherty SJ, Fahey DW, Forster PM, Berntsen T, DeAngelo BJ, et al. Bounding the role of black carbon in the climate system: A scientific assessment. J Geophys Res Atmos 2013;118(11):5380–552.
[3] Fahey DW, S.J. Doherty, K.A. Hibbard, A. Romanou, P.C. Taylor. Physical drivers of climate change. 2017.
[4] Pucher G, Allan W, Poitras P. Characteristics of deposits in gas turbine combustion chambers using synthetic and conventional jet fuels. J Eng Gas Turbines Power 2013;135(7).
[5] ICAO Environmental report 2016Technical Report; 2016.
[6] F. Rodríguez YB, J. Dornoff, P. Mock Recommendations for post-euro 6 standards for light-duty vehicles in the european union. Communications 2019; 49(30): 847129-102.
[7] Dooley S, Won SH, Heyne J, Farouk TI, Ju Y, Dryer FL, et al. The experimental evaluation of a methodology for surrogate fuel formulation to emulate gas phase combustion kinetic phenomena. Combust Flame 2012;159(4):1444–66.
[8] Yu W, Yang W, Tay K, Zhao F. An optimization method for formulating model-based jet fuel surrogate by emulating physical, gas phase chemical properties and threshold sooting index (TSI) of real jet fuel under engine relevant conditions. Combust Flame 2018;193:192–217.
[9] Mensch A, Santoro RJ, Litzinger TA, Lee SY. Sooting characteristics of surrogates for jet fuels. Combust Flame 2010;157(6):1097–105.
[10] Honnet S, Seshadri K, Niemann U, Peters N. A surrogate fuel for kerosene. P Combust Inst 2009;32(1):485–92.
[11] Yu B, Jiang X, He D, Wang C, Wang Z, Cai Y, et al. Development of a Chemical-Kinetic Mechanism of a Four-Component Surrogate Fuel for RP-3 Kerosene. ACS Omega 2021;6(36):23485–94.
[12] Yu Z, Wei S, Wu C, Wu L, Sun L, Zhang Z. Development and verification of RP-3 aviation kerosene surrogate fuel models using a genetic algorithm. Fuel 2022;312: 122853.
[13] Liu J, Hu E, Zeng W, Zheng W. A new surrogate fuel for emulating the physical and chemical properties of RP-3 kerosene. Fuel 2020;259:116210.
[14] Mao Y, Xia J, Ruan C, Wu Z, Feng Y, Zhu J, et al. An experimental and kinetic modeling study of a four-component surrogate fuel for RP-3 kerosene. P Combust Inst 2021;38(1):555–63.
[15] Gao Z, Cheng X, Ren F, Zhu L, Huang Z. Compositional Effects on Sooting Tendencies of Diesel Surrogate Fuels with Four Components. Energ Fuel 2020;34 (7):8796–807.
[16] Pelucchi M, Oßwald P, Pejpichestakul W, Frassoldati A, Mehl M. On the combustion and sooting behavior of standard and hydro-treated jet fuels: An experimental and modeling study on the compositional effects. P Combust Inst 2021;38(1):523–32.
[17] He Y, Qi S, Liu S, Xin S, Zhu Y, Wang Z. Effects of the Gas Preheat Temperature and Nitrogen Dilution on Soot Formation in Co-flow Methane, Ethane, and Propane Diffusion Flames. Energ Fuel 2021;35(9):7169–78.
[18] Qi S, Sun Z, Wang Z, Liu Y, He Y, Liu S, et al. Effects of gas preheat temperature on soot formation in co-flow methane and ethylene diffusion flames. P Combust Inst 2021;38(1):1225–32.
[19] Chu C, Zaher MH, Thomson MJ. The temperature dependence of soot formation in laminar coflow aromatic flames. Combust Flame 2022;241:112074.
[20] Chu C, Amidpour Y, Eaves NA, Thomson MJ. An experimental and numerical study of the effects of reactant temperatures on soot formation in a coflow diffusion ethylene flame. Combust Flame 2021;233:111574.
[21] Gülder ÖL. Soot formation in laminar diffusion flames at elevated temperatures. Combust Flame 1992;88(1):75–82.
[22] Gomez A, Sidebotham G, Glassman I. Sooting behavior in temperature-controlled laminar diffusion flames. Combust Flame 1984;58(1):45–57.
[23] Michelsen HA, Schulz C, Smallwood GJ, Will S. Laser-induced incandescence: Particulate diagnostics for combustion, atmospheric, and industrial applications. Progress Energy Combust Sci 2015;51:2–48.
[24] Liu F, Snelling DR, Thomson KA, Smallwood GJ. Sensitivity and relative error analyses of soot temperature and volume fraction determined by two-color LII. Appl Phys B-Lasers O 2009;96(4):623–36.
[25] Orain M, Baranger P, Ledier C, Apeloig J, Grisch F. Fluorescence spectroscopy of kerosene vapour at high temperatures and pressures: potential for gas turbines measurements. Appl Phys B 2014;116(3):729–45.
[26] Mouis AG, Menon A, Katta V, Litzinger TA, Linevsky M, Santoro RJ, et al. Effects of m-xylene on aromatics and soot in laminar, N2-diluted ethylene co-flow diffusion flames from 1 to 5atm. Combust Flame 2012;159(10):3168–78.
[27] Zhang Y, Xiao B, Li Y, Liu P, Zhan R, Huang Z, et al. LIF diagnostics for selective and quantitative measurement of PAHs in laminar premixed flames. Combust Flame 2020;222:5–17.
[28] Zhang Y, Li Y, Wang L, Liu P, Zhan R, Huang Z, et al. Investigation on the LIF spectrum superposition of gas-phase PAH mixtures at elevated temperatures: potential for the analysis of PAH LIF spectra in sooting flames. Appl Phys B 2019; 125(5):72.
[29] Zhang Y, Liu P, Li Y, Zhan R, Huang Z, Lin H. Study on fluorescence spectroscopy of PAHs with different molecular structures using laser-induced fluorescence (LIF) measurement and TD-DFT calculation. Spectrochim Acta A Mol Biomol Spectrosc 2020;224:117450.
[30] Zhang Y, Wang L, Liu P, Li Y, Zhan R, Huang Z, et al. Measurement and extrapolation modeling of PAH laser-induced fluorescence spectra at elevated temperatures. Appl Phys B 2018;125(1):6.
[31] Liu P, He Z, Hou G-L, Guan B, Lin H, Huang Z. The Diagnostics of Laser-Induced Fluorescence (LIF) Spectra of PAHs in Flame with TD-DFT: Special Focus on Five-Membered Ring. Chem A Eur J 2015;119(52):13009–17.
[32] Frenklach M, Mebel AM. On the mechanism of soot nucleation. Phys Chem Chem Phys 2020;22(9):5314–31.
[33] Sirignano M, Bartos D, Conturso M, Dunn M, D'Anna A, Masri AR. Detection of nanostructures and soot in laminar premixed flames. Combust Flame 2017;176: 299–308.

[34] Steinmetz SA, Ahmed HA, Boyette WR, Dunn MJ, Roberts WL, Masri AR. Effects of ammonia and hydrogen on the sooting characteristics of laminar coflow flames of ethylene and methane. Fuel 2022;307:121914.
[35] Dasch CJ. One-dimensional tomography - a comparison of abel, onion-peeling, and filtered backprojection methods. Appl Optics 1992;31(8):1146–52.
[36] ANSYSChemkin 17.0 (15151). Reaction Design, San Diego 2015.
[37] Gao Z, Zhu L, Zou X, Liu C, Tian B, Huang Z. Soot reduction effects of dibutyl ether (DBE) addition to a biodiesel surrogate in laminar coflow diffusion flames. P Combust Inst 2019;37(1):1265–72.
[38] Ranzi E, Frassoldati A, Grana R, Cuoci A, Faravelli T, Kelley AP, et al. Hierarchical and comparative kinetic modeling of laminar flame speeds of hydrocarbon and oxygenated fuels. Progress Energy Combust Sci 2012;38(4):468–501.
[39] China National Standardization Technical Committee on Petroleum Products and Lubricants. NO.3 Jet fuel. GB/T 6537-2006[S]. Beijing Standards Press of China 2007:1-5.(in Chinese).
[40] Jiang L, Gu C, Huo J, Yang W. Improved Two-Color Method for Temperature Measurement of Soot Flames. J Thermophys Heat Tr 2021;36(2):431–9.
[41] Smooke MD, McEnally CS, Pfefferle LD, Hall RJ, Colket MB. Computational and experimental study of soot formation in a coflow, laminar diffusion flame. Combust Flame 1999;117(1):117–39.
[42] Wu J, Chen L, Bengtsson P-E, Zhou J, Zhang J, Wu X, et al. Effects of carbon dioxide addition to fuel on soot evolution in ethylene and propane diffusion flames. Combust Flame 2019;199:85–95.
[43] Roper FG. Prediction of laminar jet diffusion flame sizes. 1. Theoretical-model. Combust Flame 1977;29(3):219–26.
[44] Roper FG, Smith C, Cunningham AC. Prediction of laminar jet diffusion flame sizes. 2. Experimental-verification. Combust Flame 1977;29(3):227–34.
[45] Snelling DR, Liu F, Smallwood GJ, Gülder ÖL. Determination of the soot absorption function and thermal accommodation coefficient using low-fluence LII in a laminar coflow ethylene diffusion flame. Combust Flame 2004;136(1):180–90.
[46] Santoro RJ, Yeh TT, Horvath JJ, Semerjian HG. The Transport and Growth of Soot Particles in Laminar Diffusion Flames. Combust Sci Technol 1987;53(2–3):89–115.
[47] Kang Y, Sun Y, Lu X, Gou X, Sun S, Yan J, et al. Soot formation characteristics of ethylene premixed burner-stabilized stagnation flame with dimethyl ether addition. Energy 2018;150:709–21.
[48] Hua Y, Qiu L, Liu F, Qian Y, Meng S. Numerical investigation into the effects of oxygen concentration on flame characteristics and soot formation in diffusion and partially premixed flames. Fuel 2020;268:117398.
[49] Frenklach M, Wang H. Detailed modeling of soot particle nucleation and growth. Symp (Int) Combust 1991;23(1):1559–66.